

Miniature Augmentation Sensors for Integrated Inertial/GPS Based Navigation Applications

Ralph E. Hopkins, Donald E. Gustafson, Peter Sherman

Charles Stark Draper Laboratory
555 Technology Square
Cambridge, MA 02139
USA

rhopkins@draper.com

ABSTRACT

Recent developments in the miniaturization of inertial instruments and GPS receiver hardware have led to the introduction of small, low cost integrated navigation systems which advertise better than 10 m position accuracy under circumstances where GPS remains available. Under situations where GPS is unavailable or intermittent such as urban, indoor or subterranean environments, navigation performance is limited by inertial sensor performance. Given the size, power and cost constraints of miniature systems, currently only tactical grade MEMS gyros and accelerometers (performing at around 1 deg/h and 1 milli-g bias stabilities, respectively) are suitable for use in these applications. Consequently position accuracy rapidly degrades in a tactical grade inertial/GPS system when GPS is denied. To recover navigation accuracy in miniature systems then, it is necessary to use additional sensors (e.g., velocity meters, magnetometers, barometers) and algorithms to augment the inertial system.

This paper discusses some of the ongoing activities in the technology development of miniature augmentation sensors that could be used to improve performance in applications with little or no GPS signal. Current developments in miniature magnetometers, velocity meter technologies and MEMS precision clocks and MEMS barometers are discussed with emphasis on suitability for navigation system integration. Recent advances in optical sensors, in particular 3D cameras, are also discussed with some references to advanced inertial aiding approaches. Simulations of position error over time are compared for certain GPS-unavailable missions based on hypothetical IMU performance expected from these inertial sensors, with and without a velocity meter, and with/without barometer and magnetometer. Algorithms used to implement integration of barometers and magnetometers into the INS navigation solution are also presented. The paper concludes with test results demonstrating a prototype miniature navigation system developed for personal, land navigation applications.

INTRODUCTION

Recent developments in the miniaturization of inertial instruments and GPS receiver hardware have led to the introduction of small, low cost integrated navigation systems such as the Integrated Guidance Systems LLC IGS-200 series and Atlantic Inertial Systems SiNAV products (Fig 1a – 1b). In applications where GPS remains available, these systems advertise position accuracy of approximately 4 to 10 m. (Ref [1,2]). Under situations where GPS is denied, compromised (e.g. multipath) or intermittent, position accuracy degrades as error growth from the inertial sensors dominates the dead reckoning navigation solution.



Figure 1a: IGS-200 Series Navigation System Ref [1].



Figure 1b: AIS SiNAV Navigation System Ref [2].

There are many emerging mission applications for GPS-unavailable navigators; typical missions are personal navigation in urban (indoor and outdoor) environments, search and rescue robots in difficult access (e.g., rubble) environments, autonomous land vehicle in urban or rural environments, and autonomous underwater vehicles in littoral or deep ocean environments. Typical position knowledge desired is 1 to 3 meters over periods of minutes to hours, under operational temperatures from -25 to +130 degrees F and rate and acceleration measurement ranges up to 360 deg/s and 5g. Table 1 presents a summary of several mission requirement goals for urban and subterranean/sub-ocean environments.

Table 1: Mission Requirement Goals.

Goals	Mission					
	Urban Personal Navigation System	Subterranean Personal Navigation System		Search & Rescue Robot	Autonomous Land Vehicle	Autonomous Undersea Vehicle
Size (in ³)	10	12		4	25	25
Weight (lb)	0.5	3		1	2	2
Power (w)	5	5		1	20	20
GPS Availability	Intermittent	Denied		Denied	Intermittent	Denied
Mission Time (h)	No Limit	0.5	8	1	1	8
Position Knowledge (meters)	3	3	3	1	3	10
Velocity Meter	Yes	No	Yes	Yes	Yes	Yes
Max Speed (m/s)	1	1	1	1	10	10

Currently, miniature inertial/GPS systems feature tactical grade instruments having approximately 1 deg/h (gyro) and 1 milli-g (accelerometer) bias stabilities. Unaided, the position error from 1 milli-g of accelerometer bias uncertainty alone integrates to approximately 17 m in 1 minute, and will grow by over 3 orders of magnitude in an hour. A personal navigation application where horizontal position needs to be known to 1 meter after 1 hour in the absence of GPS would require gyro and accelerometer bias performance on the order of ~5 micro-deg/hr and ~15 nano-g, respectively. No suitable (e.g., cost, size, power) inertial technology exists today that approaches this performance level. Consequently, in a GPS-denied environment,

the use of active and passive augmentation sensors (aiding devices) is required to provide velocity and/or attitude updates to bound the error due to the drift in the inertial components.

Examples of augmentation sensors are velocity sensors, odometers, baroaltimeters, magnetometers, ranging devices (i.e. optical and laser scanners), proximity sensors, and GPS pseudolites. There can also be improvements from using special procedures such as ZUPTs (Zero Velocity Updates), mapping information, or path crossings. Augmentation sensors open the door to the use of much lower performing inertial sensors, so that current technology can be applied to developing an integrated navigation solution of required accuracy.

This paper presents an overview of current developments in miniature augmentation sensor technology that are suitable for navigation system applications. Timing references, magnetometers, barometers and velocity sensors are discussed in detail, with emphasis placed on current miniaturization efforts. Recent advances in optical sensors, in particular 3D cameras, are also discussed with some references to advanced inertial aiding approaches. Some discussion of sensor integration algorithms is also presented, along with performance simulations of some candidate architectures. The paper concludes with an example of a personal navigation system which integrates multiple augmentation sensors with an inertial/GPS INS.

MINIATURE AUGMENTATION SENSORS

Among the components critical for development of a miniaturized integrated Inertial/GPS system are “augmentation” sensors such as barometers, magnetometers, velocity meters and timing references. Recent developments in MEMS and solid state optical technologies are, as is the case with inertial sensors, enabling the development of miniaturized versions of these sensors with performance suitable for integration with small INS/GPS systems. This section discusses operational principles, miniature designs and performance considerations for these sensors.

Barometers

The addition of a barometer to integrated navigation systems is not a novel idea as they are typically inserted in INS systems to constrain position error growth in the local vertical channel (Ref [10, 11, 12]). Equation [1] below shows how vertical acceleration is calculated in a local level frame:

$$\ddot{h} = A_{ZSF} - g - \omega_E V_N + (\Omega_N + \omega_N) V_E \quad [1]$$

where:

- \ddot{h} = Indicated z-axis (vertical) acceleration
- A_{ZSF} = Z-axis accelerometer indicated specific force
- g = Plumb-bob local gravity
- V_N, V_E = North and East velocities relative to earth frame
- ω_N, ω_E = North and East local frame angular rates relative to earth frame
- Ω_N = North component of earth rate

Neglecting the coriolis frame-rate terms in [1] and integrating twice gives, to first order, the estimate for vertical position (h):

$$h = \iint (A_{ZSF} - g) dt dt \quad [2]$$

Equation [2] reveals the vertical channel instability problem; local gravity (g) is determined via a model in the INS flight computer, and is a function of altitude. A positive altitude error will cause an under estimate in the value of g , which subsequently leads to an increase in the positive altitude error. Likewise a negative altitude error causes an over estimate of g which further contributes the altitude under estimate. Consequently, in an inertial-only system, the vertical channel is inherently unstable with the altitude estimate diverging either positively or negatively with time.

Gravity as a function of altitude is given by:

$$g(h) = g_0 \left(1 - \frac{2h}{R} \right) \quad [3]$$

where: $g(h)$ = Plumb-bob local gravity as a function of altitude h
 g_0 = Nominal plumb-bob local gravity (9.8 m/s^2)
 h = Altitude
 R = Nominal earth radius ($6.378 \times 10^6 \text{ m}$)

From [3] then, a differential equation for altitude error can be written as (ref [12]):

$$\ddot{h}_e - \frac{2g}{R} h_e = 0 \quad [4]$$

where: h_e = altitude error

Solving [4] with a non-zero position error (h_0) initial condition gives the growth in altitude error estimate as:

$$h_e(t) = h_0 \cosh \left(\sqrt{\frac{2g_0}{R}} t \right) \quad [5]$$

Substituting numerical values into [5] shows that an initial altitude error will double after about 750 seconds unless compensated by an external sensor such as a barometer.

Consequently barometer integration is used extensively in INS system design. Likewise GPS receivers are incorporating barometers as a means to improve vertical channel ranging accuracy (Ref [13]). Commercial examples are the Garmin GPSMAP 76 Series receivers (fig. 2) which include a barometer whose pressure resolution capability translates into an approximately 1 foot vertical resolution capability.



Figure 2: Garmin GPS Receivers w/barometric altimeter (Ref: www.garmin.com).

Nominal sea level atmospheric pressure is approximately 0.1 MPa, and decreases exponentially with increasing altitude at a rate of approximately 10 Pa/m (ref [13]). Hence barometer sensitivity on the order of ~1 Pa enables sub-meter altitude resolution. VTI Technologies offers a line of silicon MEMS based pressure sensors such as the SCP1000 model (Fig 3) which features a 1.5 Pa resolution capability and a minimum range of 30 kPa. These limits enable use of this barometer from sea level to approximately 30,000 ft altitude, with sub-meter accuracy.



Figure 3: VTI SCP1000 Pressure Sensor (Ref: www.vti.fi).

The VTI **MEMS pressure sensors** have the familiar silicon capacitive architecture used in many MEMS sensor designs; two parallel plates form a capacitive gap, which changes with relative deflection under applied pressure. VTI employs an advanced Chip-on-MEMS packaging process that enables a heterogeneous, wafer-level integration of the MEMS sensor with ASIC electronics, resulting in a compact (approx. 4 mm x 4 mm x 1mm) low cost sensor/electronics chipset (Fig 4. Ref [14]) ideally suited for miniature INS system integration.

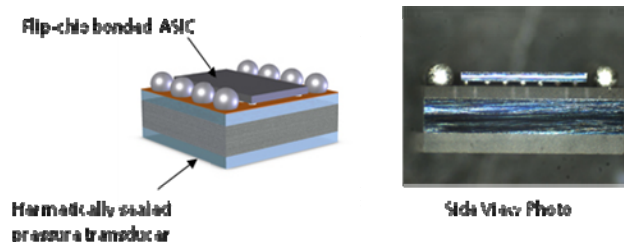


Figure 4: VTI Chip-on-MEMS Process (Ref: www.vti.fi).

Reference [13] presents a method for integrating a barometer into the vertical channel with error states modeled for barometer bias and scale factor. Equation [6] below shows the error state model for the navigation system vertical channel:

$$\begin{bmatrix} \dot{\delta h} \\ \dot{\delta V} \\ \dot{B} \\ \dot{S} \end{bmatrix} = \begin{bmatrix} 0 & 1 & 0 & 0 \\ 2\omega_s^2 & 0 & 0 & 0 \\ 0 & 0 & -1/\tau & 0 \\ 0 & 0 & 0 & 0 \end{bmatrix} \begin{bmatrix} \delta h \\ \delta V \\ B \\ S \end{bmatrix} + \begin{bmatrix} 0 & 0 \\ 1 & 0 \\ 0 & 1 \\ 0 & 0 \end{bmatrix} \begin{bmatrix} \delta a \\ \omega \end{bmatrix} \quad [6]$$

where:

- δh = altitude error
- δV = vertical axis velocity error
- B = barometer bias error
- S = barometer scale factor error
- ω_s = Schuler frequency = $\sqrt{(g/R)}$, ref equation (6)
- τ = bias error time constant, ref equation (9)
- ω = bias error Gaussian noise, ref equation (9)
- δa = vertical acceleration Gaussian noise

The barometer scale factor error in [6] is assumed fixed, and the bias is modeled as a first order Markov process according to:

$$\dot{B} + \frac{1}{\tau} B = \omega \quad [7]$$

where:

- B = barometer bias error
- τ = bias error time constant
- ω = bias error Gaussian noise

The barometer observation model equation is then given by:

$$y_{baro} = \begin{bmatrix} 1 & 0 & -1 & -h \end{bmatrix} \begin{bmatrix} \delta h \\ \delta V \\ B \\ S \end{bmatrix} + v_{baro} \quad [8]$$

where:

- y_{baro} = barometer observation model output
- v_{baro} = barometer noise
- h = vertical altitude estimate

Magnetometers

Magnetometers are used to augment the heading information in integrated navigation systems by furnishing orientation with respect to earth's magnetic field. Magnetometers are available in many designs employing different technologies. Figure 5 below (adapted from ref [4]) shows that the performance range of different magnetometer technologies spans approximately six orders of magnitude, starting with Hall sensors at the coarse end, to Superconducting Quantum Interference Device (SQUID) designs at the very high sensitivity end of the spectrum.

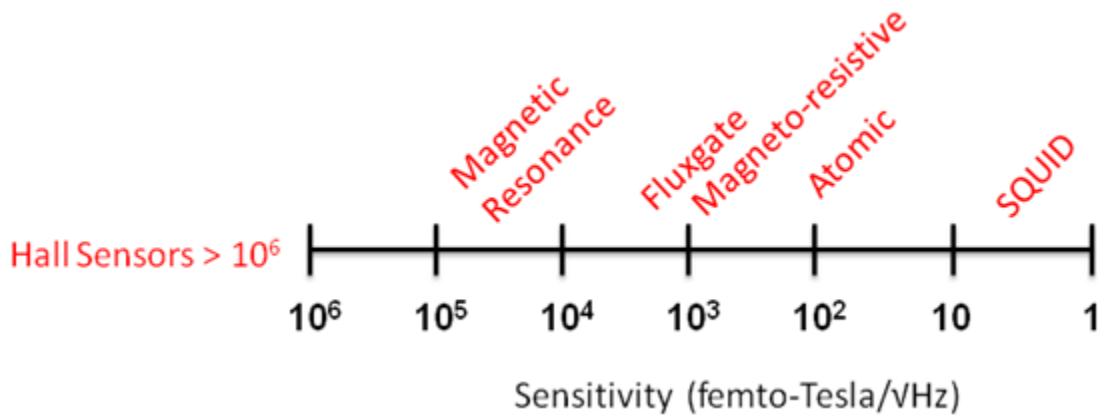


Figure 5: Magnetometer Technologies v. Performance.

Because of the need to cool SQUID devices to cryogenic temperature, their application is limited to laboratory and clinical settings such as in hospital MRI imaging systems.

The next most precise technology is **atomic** (sometimes referred to as quantum) magnetometers. Functionally an atomic magnetometer detects the presence of magnetic fields via their interaction with a gas filled vapor cell (see Fig. 6). The gaseous media, typically an alkali metal such as potassium, cesium or rubidium, is optically pumped to an excited state, and the magnetic spin moment of the atoms aligns with the optical source, allowing transmission of the light to a photodetector. An externally applied magnetic field disrupts the alignment of the vapor magnetic spin vectors causing an increase in the gas absorption of the light source, and a decrease in the light intensity observed at the photodetector. Precision sensing is achieved via application of a frequency controlled RF source which modulates the magnetic spin moment alignment of the gas and the transparency of the vapor cell. The modulation frequency is servo controlled to maintain a null at the photodetector; an externally applied magnetic field introduces a change in the gas vapor transmission which is restored by a shift in the servo controlled RF frequency. The frequency shift caused by the ambient magnetic field is called the Larmor frequency, and is proportional to the magnitude of the applied magnetic field.

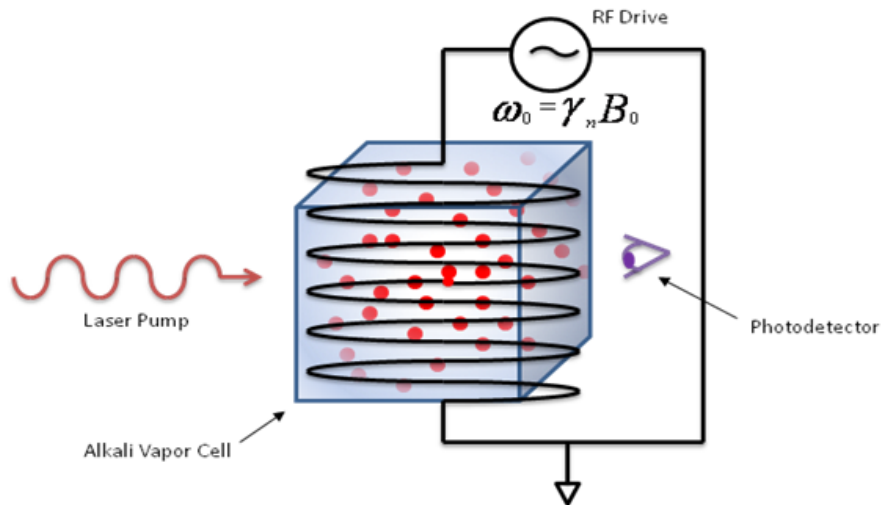


Figure 6: Schematic of Atomic Magnetometer.

Currently atomic magnetometers, such as the one shown in Fig. 7 offered by GEM Systems, Markham, Ontario, are large-sized devices designed for specialized geo-physical survey applications.



Figure 7: GEM GSM-19W Magnetometer system, configured with 2 sensors for gradient measurements (Ref [28]).

However, recent advances in MEMS technologies are enabling the development of miniaturized atomic magnetometers. Figure 8 below shows a ultra small scale magnetometer under development at NIST (Ref [4]) which demonstrates the potential for achieving very high performance in a miniature package size.

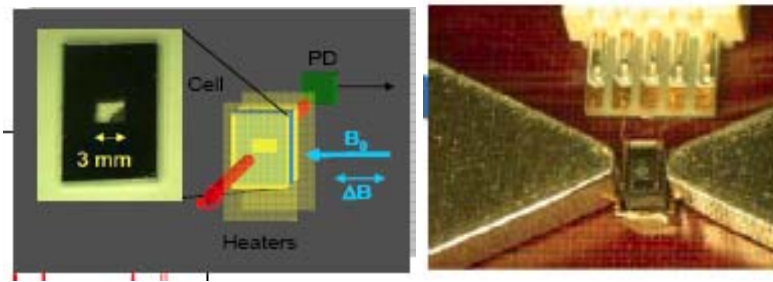


Figure 8: NIST Miniature Atomic Magnetometer (Ref [4]).

Until miniature atomic magnetometers transition from laboratory demonstration units to a mass produced product, fluxgate and/or magnetoresistive designs are a better suited magnetometer technology for a miniature navigation system. **Magnetoresistive** sensors employ a nickel-iron thin film patterned as a resistive element in a Wheatstone bridge configuration (ref [9]). Under an applied external magnetic field, the magnetization vector of the NiFe film aligns with the current flow, and causes a change in the net electrical resistance of the element (Fig 9a, 9b). An example of a magneto-resistive based magnetometer is the Honeywell HMC 1043, which features a triad sensor arrangement in a single, compact 3 mm x 3mm package (ref [26]). Hence, the triad of bridge sensors can be calibrated to determine the net magnetic field vector components.

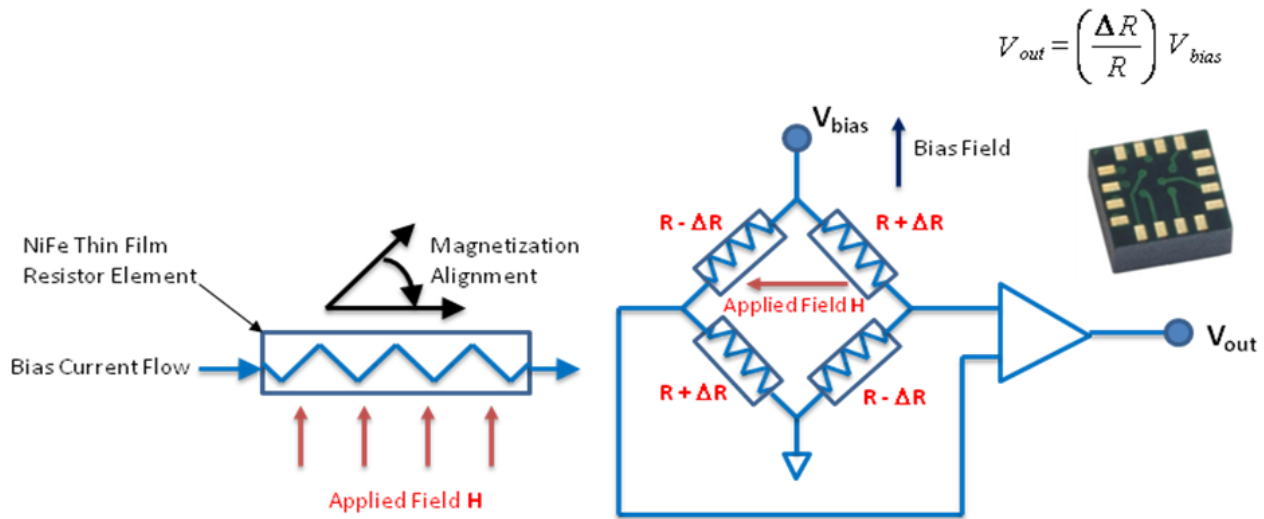


Figure 9a: Magneto-resistive Element.

Figure 9b: Schematic and Honeywell HMC1043.

Requirements on the performance of a magnetometer for use in a navigation system are driven by scaling of magnetic field strength as the sensor is rotated from magnetic north to magnetic east. In the mid-latitude area of the northern hemisphere, the scaling is about 270 nT/deg. Noise equivalent resolution of 0.1deg/√Hz requires a sensor noise floor of 27nT/√Hz, the Honeywell HMC 1043 resolution is specified at 12 nT/√Hz.

Figure 10 below shows the basic **fluxgate** magnetometer design concept (example ref [6]), a technology which has similar sensitivity as magnetoresistive sensors. A magnetic core material is wound with a set of drive and sense coils; application of AC current to the drive induces an alternating magnetic field that induces

an AC output voltage in the sense coil, which is symmetric about zero in the absence of external magnetic fields. The application of an external magnetic field biases the AC output voltage and produces a net differential output in the magnetometer proportional to the strength of the applied field. Fluxgate designs are sensitive to magnetic fields applied along the central core axis; hence a triad is required to resolve magnetic field orientation.

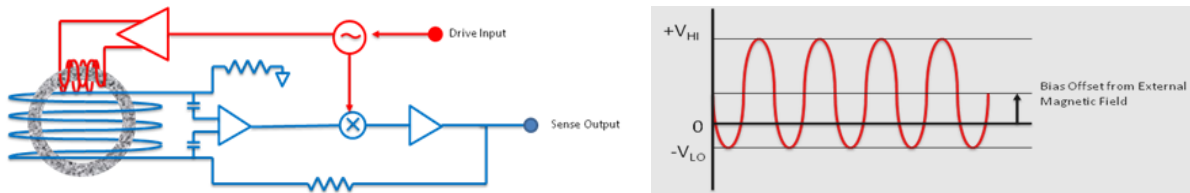


Figure 10: Fluxgate Magnetometer Schematic.

The PNI Sensor Corporation (Santa Rosa, CA, www.pnicorp.com) offers several models of magnetometers suitable for inertial system augmentation. For example, their TCM 5 and TCM 6 models (Fig. 11 ref [7]) are full 3-axis modules with integrated MEMS accelerometers for tilt compensation. The three-axis module design enables determination of magnetic north through simple trigonometric computations. Magnetic north heading can be converted to a true north frame by adding a declination angle from a database reference such as the World Magnetic Model (ref [8]).



Figure 11: PNI TCM 5 and TCM 6 Magnetometer Modules (Ref [26]).

The presence of anomalous magnetic fields and the influence of neighboring magnetic materials can corrupt the magnetometers indication of heading and present a challenge when developing the integrated navigation solution. REF [31].

Some magnetometers offer a self-compensation capability to address this difficulty. For example, the TCM series magnetometers (nominally a 0.1° accuracy sensor) feature a digitally enabled compensation capability to account for the magnetic field distortion of neighboring hard and soft magnetic materials. Hard magnetic materials maintain their north-south polarity with orientation. Compensation for hard magnetic distortion can be implemented using the the form of (ref [29]):

$$\Delta\psi_m = H_x \cos\psi_m + H_y \sin\psi_m \quad [9]$$

where: ψ_m = magnetic heading angle
 $\Delta\psi_m$ = magnetic heading error
 H_x, H_y = x and y axis calibration coefficients

Soft magnetic materials are re-magnetized with orientation changes with respect to Earth's field which alters the functional form of the compensation approach to (ref [29]):

$$\Delta\psi_m = S_x \cos 2\psi_m + S_y \sin 2\psi_m \quad [10]$$

where: ψ_m = magnetic heading angle
 $\Delta\psi_m$ = magnetic heading error
 S_x, S_y = x and y axis calibration coefficients

A pair of hard and soft iron compensation coefficients could be defined mathematically for each axis, however each of these 12 coefficients may not be independently observable.

An example of magnetometer heading measurement corruption is shown in the plots in Figure 12 where the "true" inertial heading (red) and magnetic indicated heading (blue) are contrasted. This data was taken from the prototype personal navigation system discussed at the end of this paper. The top plot contains data from an open field athletic track; the middle plot depicts an Urban Canyon area, and bottom plot represents indoors in a metal frame building. The vertical scales in all three are the same, 45°/division. The progression shows increasing magnetic anomalies going from open field to indoors.

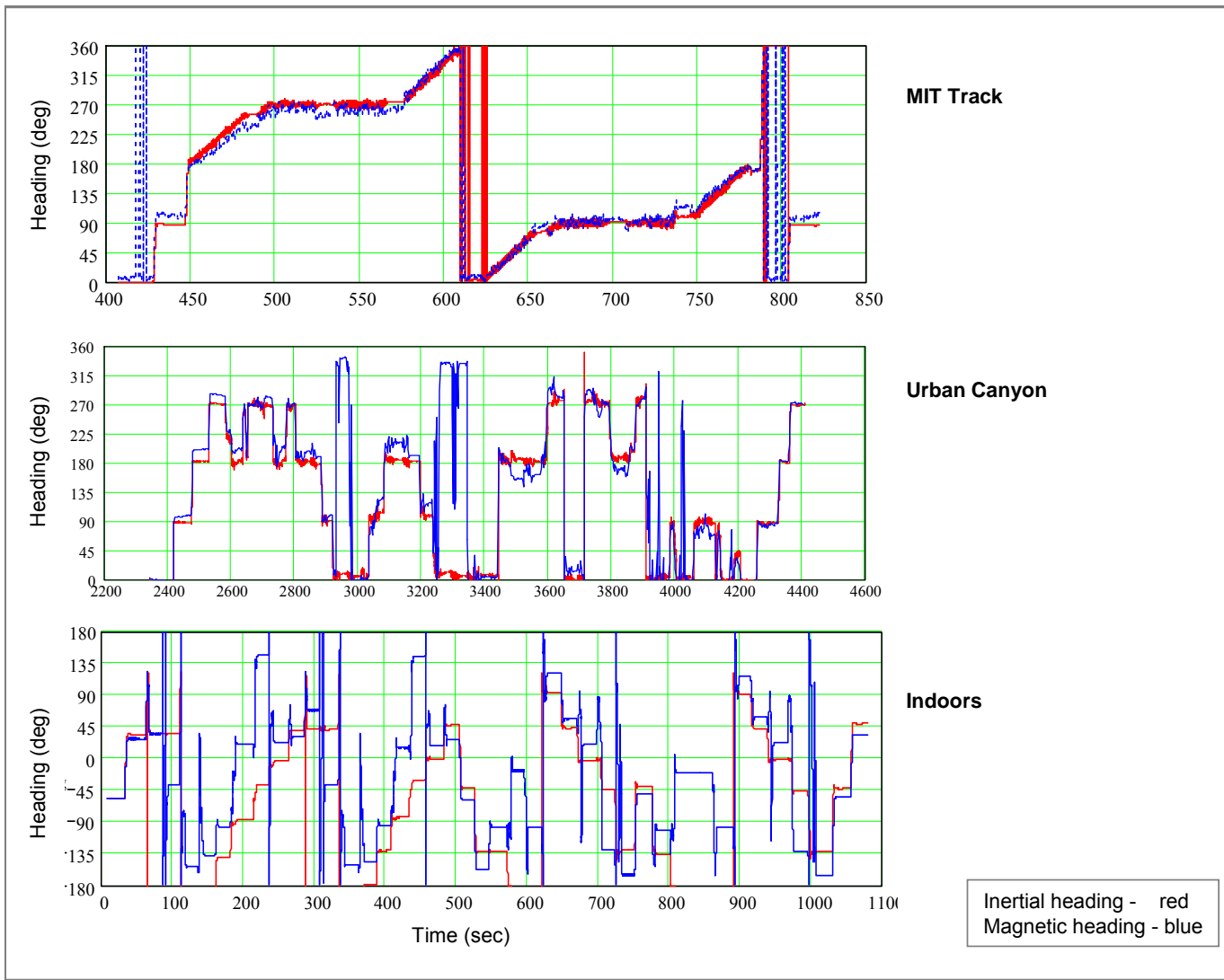


Figure 12: Magnetic v. Inertial Heading.

This data highlights the challenges for using magnetic sensing in a dead reckoning system in discriminating valid (i.e. model following) measurements from anomalous ones. Reference [8] suggests a pre-filtering approach to rejecting local magnetic anomalies, where magnetometer readings are rejected if: 1) the magnetometer indicated heading differs from the inertial indicated heading by more than three standard deviations, or 2) if indicated magnetic flux density exceeds its average value by a certain factor.

Timing Clocks

In all applications a small, low power, highly **accurate clock** is required for processing purposes. Aside from needing a high quality timing reference to compute accurate inertial estimates of velocity, position and attitude, a high performance oscillator also aids rapid re-acquisition of GPS across signal interruptions (Ref [31]). Reference [22] describes a miniature atomic clock (MAC) under development as an intermediate step

towards a full chip scale atomic clock (CSAC). The MAC is a complete packaged atomic clock with overall size 10 cm^3 and power consumption $<200 \text{ mW}$ that employs similar technology as the miniaturized atomic magnetometer discussed earlier. The CSAC program was a DARPA initiative that funded multiple teams with the objective of developing a miniature timing reference with volume $<1 \text{ cm}^3$ and power $<30 \text{ mW}$ with a timing frequency stability of 1 part in 10^{11} over an hour [Ref 23].

The MAC described in references [22, 24] is a collaborative effort between Symmetricom, Draper Laboratory, and Sandia National Lab and is shown schematically in figure 13.

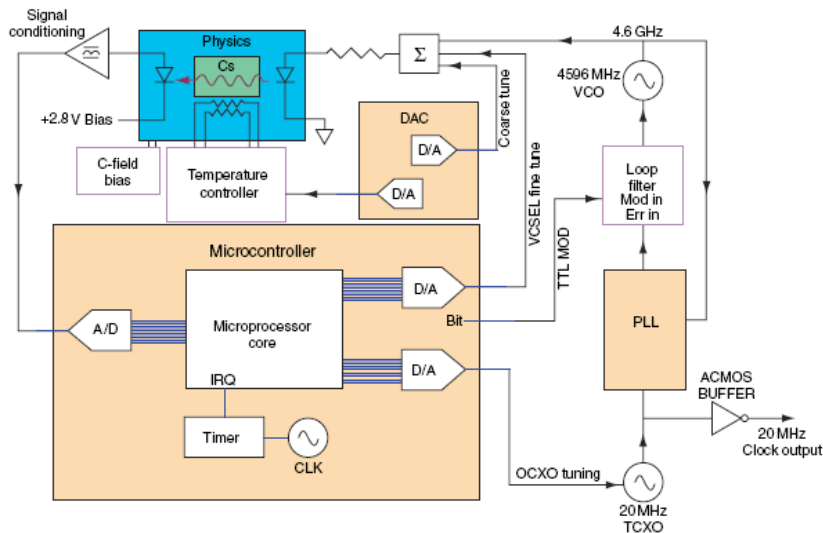


Figure 13: Miniature Atomic Clock (MAC) Schematic (Ref [25]).

Like the atomic magnetometer discussed above, RF transmission through an alkali cell (cesium) serves as the fundamental sensor building block. Here, an optical pump energizes electrons in the two lower spectral ground states of the cesium gas. The application of a microwave tuned to the ground state transition frequency (4.6 GHz) introduces a redistribution of electrons in the two ground states; this resonance interaction alters the absorption properties of the cesium gas causing a decrease in sensed RF power at a photodetector. Servo-electronics controls a VCO to keep the microwave source tuned to the atomic transition frequency, an exceptionally stable reference.

Atomic clocks operating on the above principle have historically been large ($>100 \text{ cm}^3$) high power ($>5 \text{ W}$) systems. The MAC team has employed MEMS and solid state optical technologies to enable significant miniaturization as shown in figs 14a-14b.

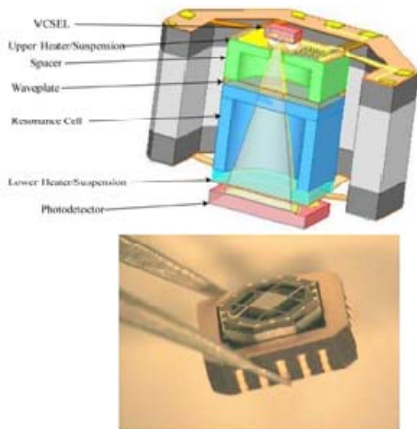


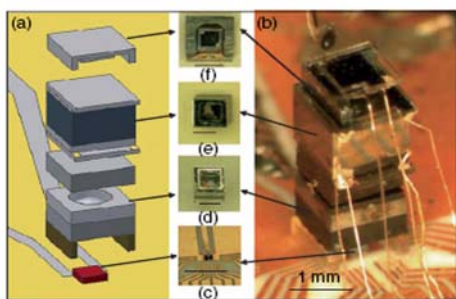
Figure 14a: MAC Physics Package (Ref [24, 25]).



Figure 14b: Prototype MAC Electronics Module (Ref [24]).

Rather than a high powered optical lamp, a vertical cavity surface emitting laser VCSEL (< 2 mW) is used as optical pump, and is integrated directly into a MEMS fabricated cesium cell with a folded optics configuration to achieve very small size. Prototype versions of the MAC have demonstrated long term (200 day) frequency stability of 10^{-10} Ref [24].

Likewise, NIST has a CSAC (ref [4, 5, 6]) under development that employs similar atomic transition technology. Like the MAC, it employs a VCSEL to minimize size and power and uses MEMS processing in its assembly. Figures 15a-15b (ref [25]) below show the physics package schematic and prototype hardware fabricated via MEMS wafer scale processing.



(a) Schematic and (b) photograph of a CSAC physics package consisting of (c) VCSEL laser source (d) optics package (e) gas vapor cell (f) photodetector

Figure 15a: NIST CSAC Physics Package (Ref [25]).

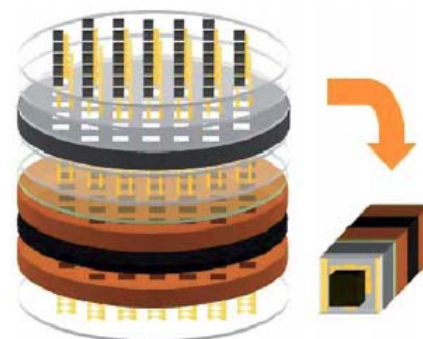


Figure 15b: Wafer scale CSAC MEMS Processing (Ref [25]).

Velocity Meters

The addition of a velocity meter is effective at bounding position error drift caused by inertial errors when GPS is unavailable; this will be discussed in further detail later in this paper. Velocity sensing can be

accomplished in the optical domain with laser Doppler radar (i.e. **LIDAR**), through RF band or ultrasonic Doppler radar. Reference [15] discusses an example of a LIDAR based velocimeter, used to furnish landing speed information for spacecraft terminal descent control on planetary landers. A schematic is shown in fig. 16; the front end of this sensor includes a diode-pumped erbium doped fiber laser, a lithium niobate waveguide electro-optic phase modulator, fiber optic couplers and splitters, and individual transmit and receive telescopes. This integrated diode assembly feeds the front end of a low noise amplifier which outputs to digital tracking filters and a controller to extract both relative velocity and range to the target surface.

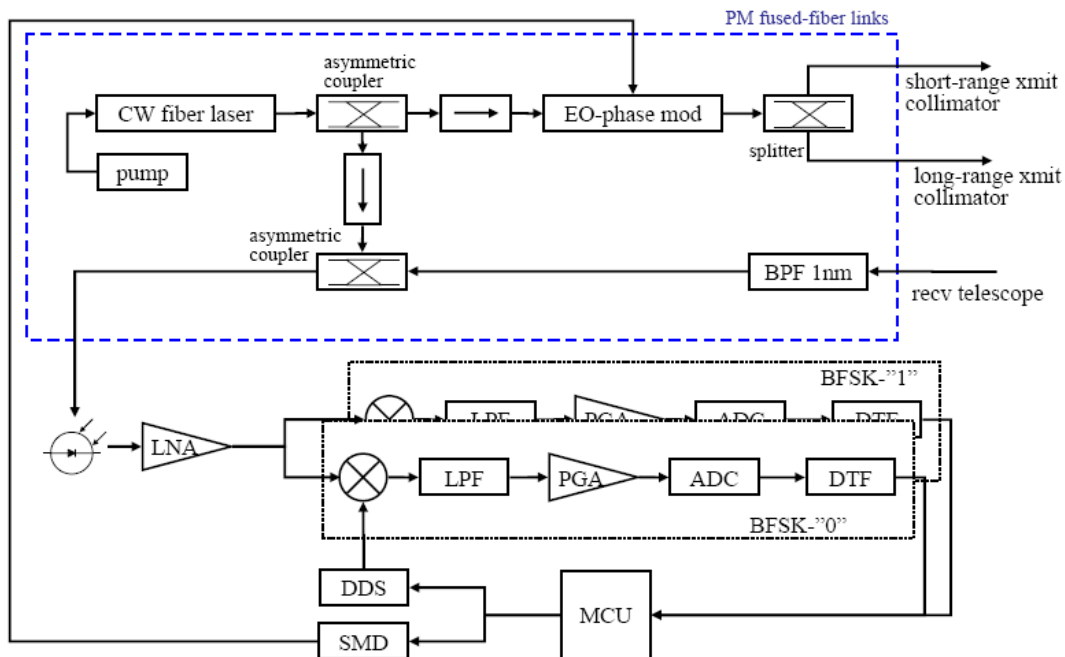


Figure 16: Miniature Coherent Velocimeter and Altimeter (MCVA) (Ref [15]).

Performance objectives of this combination system are <10 cm/s velocity and <10 m range; weight is approximately 1 kg and power is approximately 0.1 W.

The above example LIDAR based system has excellent performance, but it is unsuitable for a miniature integrated navigation system application because of size and weight considerations. In contrast, progress in miniaturization of RF patch antennas is enabling the introduction of **RF-based radar velocimeters** in miniaturized integrated navigation systems. The 24 GHz technology used in COTS traffic enforcement systems can be adapted for navigation system velocity aiding.

Figure 17 shows a basic patch antenna element produced by InnoSenT GmbH (www.innosent.de) with corresponding schematic. The patch array shown has separate transmit and receive antennas, demodulating the received signal in-phase and in quadrature with the transmission signal enables determination of the sign of the velocity measurement (i.e. sensed object moving toward or away from sensor).

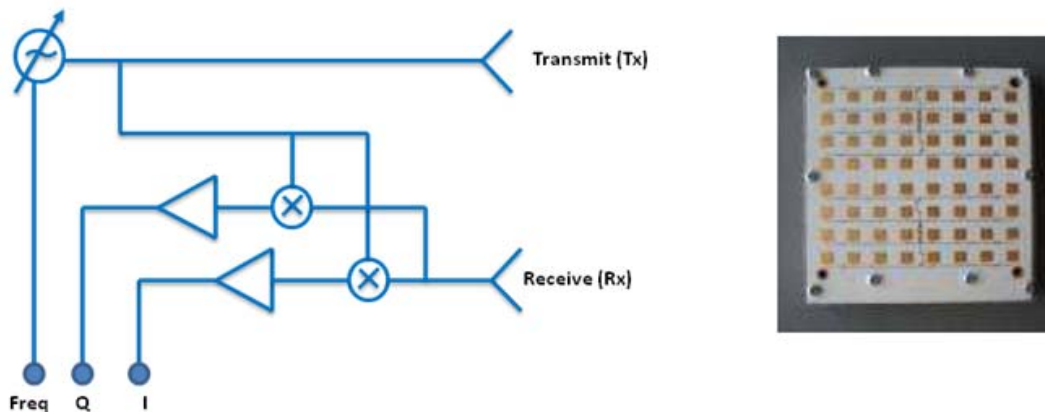


Figure 17: Basic Transmit and Receive Radar sensor with InnoSenT 8x8 Patch Array (Approx. 3 in x 3 in).

Draper Laboratory has demonstrated a prototype Personal Navigation System (ref [27]) employing RF radar technology as a velocity aiding sensor. Accuracy on the order of 1-2 cm/sec was demonstrated, with patch antennas of the size shown above in fig. 17. A broad antenna aperture size (i.e. area) helps to suppress side-lobing and control the forward projected beam-width of the radar signal. For precision velocity sensing in a navigation application, a narrow beam-width is desirable to minimize errors from side-lobe reflections so that a well defined velocity vector can be computed.

The most straightforward way to reduce RF velocimeter size while maintaining beam aperture is to increase carrier frequency. Selection of 76 GHz gives a 9:1 decrease in footprint from 24 GHz and leverages availability of components and fabrication techniques developed for automotive collision avoidance and cruise control radars. Though power efficiency is poorer at this higher frequency, net power consumption is low for this application due to the very close proximity of the sensor to ground target.

A prototype 76 GHz Doppler radar front-end was developed for Draper Laboratory by Epsilon-Lambda Electronics. A trade study was performed to determine the most power efficient mechanism for generating the carrier. Quiet oscillator sources were available at lower frequencies, but efficiencies of multipliers were poor. The design approach chosen was to use a discrete oscillator based on Gunn diode technology with direct generation of the 76 GHz carrier. The diode is mounted in a tuned cavity. A waveguide port from the cavity is matched to a micro-strip line on a printed circuit board containing the patch antenna elements and detector circuit.

In the early prototype a discrete waveguide connected the antenna to the transceiver electronics to enable independent testing of each subsystem. Later builds of the sensor integrated the electronics onto the antenna printed circuit board (PCB) (fig 18). Gain patterns for the vertical (pointing toward the waveguide, H-plane) and horizontal axes are shown. They demonstrate that the antenna can generate an isotropic pencil beam with a nominal width of 7 degrees; sidelobes are well suppressed, lower than the main beam by 16dB to 18dB.

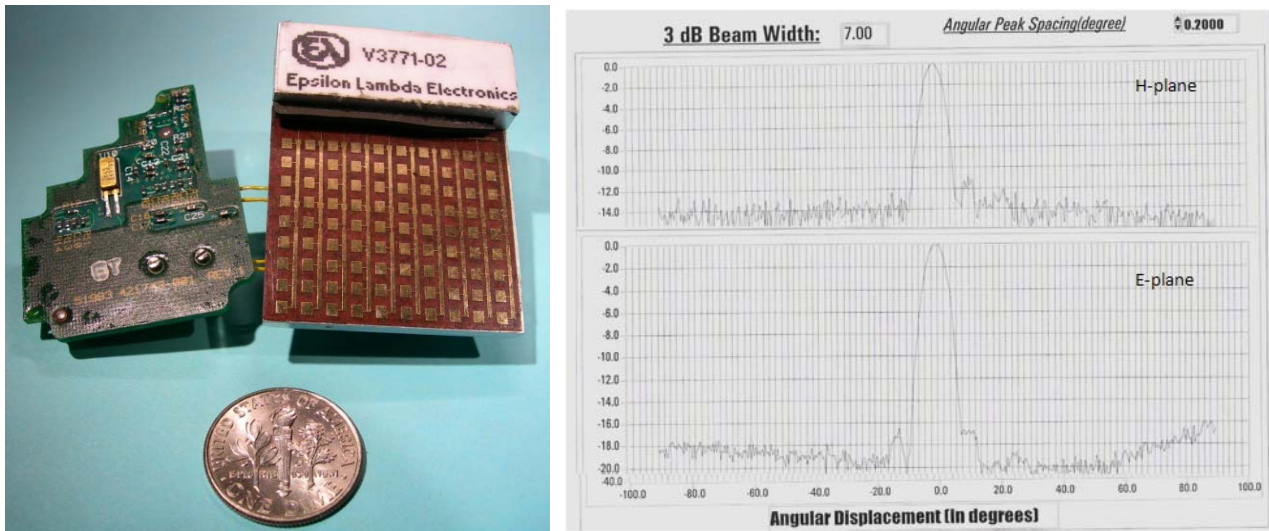


Figure 18: Integrated Doppler Transceiver and Antenna Gain Pattern.

The plots in Fig 19 show Doppler frequency shift vs. time for 24 GHz and 76 GHz sensors mounted on a cart with their beams pointed toward a set of typical ground targets. The 24 GHz shifts are scaled by the ratio of carrier frequencies. For these common surfaces, the effectiveness of target scattering between the two frequencies is qualitatively similar, indicating the capability to operate across a variety of different environments.

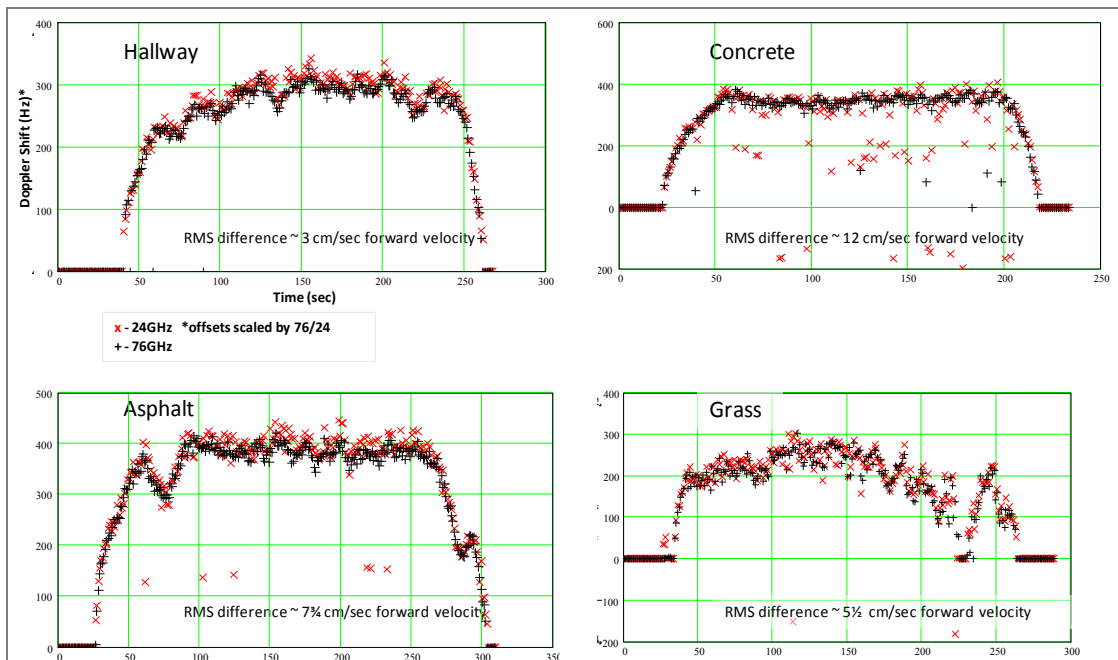


Figure 19: Measured Velocity Profiles from Common Surfaces.

Reference [16] presents an algorithm for integrating velocity measurements into a navigation solution. A simple model is used which includes velocity error and velocity white noise process terms. The velocity observation model is given by:

$$[z] = [C_e^{dopp}] [V_e \wedge] [\psi_e] - [C_e^{dopp}] [\delta V_e] + v_{dopp} \quad [11]$$

where:

- z = velocity observables in Doppler frame
- C_e^{dopp} = Doppler velocity error in earth frame
- $V_e \wedge$ = skew-symmetric matrix of the velocity vector
- ψ_e = attitude error in earth frame
- δV_e = Doppler velocity error in earth frame
- v_{dopp} = Doppler velocity noise

Note that the model includes velocity interaction with attitude errors ψ .

Doppler velocity aiding is a relatively drift-free measurement to bound drift on inertial sensors. The inertial sensors in turn provide a basis for screening Doppler measurements for spoofing by nearby moving objects or host travel in a moving vehicle. Over short timescales, inertial sensors are low drift, low noise, and unaffected by environmental factors. The navigation filter, in its sensor fusion compares each Doppler measurement to the navigation velocity, projected along the Doppler axis, and decides using a statistical criterion whether to accept the measurement or not.

An example of integration of a tactical MEMS IMU with a 76 GHz wearable radar is shown in Figure 20. Doppler velocity along a single sensor axis (blue trace) is co-plotted with inertial sensor derived velocity projected along the radar's beam (red trace). The radar is mounted to the same chassis as a tactical grade IMU; the assembly is mounted mid-body on a person walking down a city street. The two traces are well correlated. Both have the bandwidth to track velocity variations typical for a walking gait.

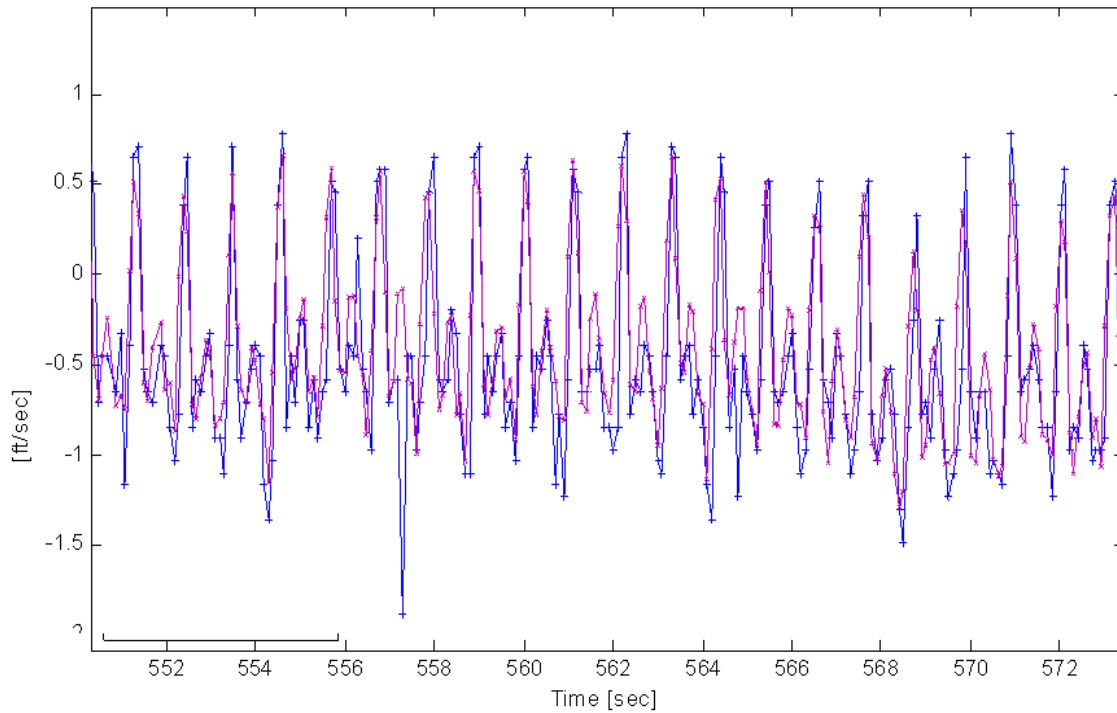


Figure 20: Inertial-derived and Velocimeter Measured Velocity Profiles.

Reference [17] presents a simpler application of velocity meters in integrated navigation systems, where a radar based sensor with two element RF patch antenna is used to furnish Zero Velocity Updates (ZUPTs) in a personal navigator system. The boot integrated ZUPT sensor shown in fig. 21 from ref [17] is used to update the navigation solution by bounding velocity error when the user is stationary.

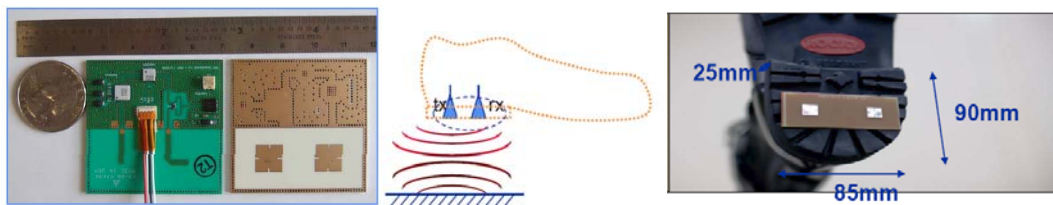


Figure 21: Boot-heel integrated RF Velocity Sensor for Personal Navigation (Ref. [17]).

This approach is a variant on a class of foot-mounted navigation systems (refs. 18-20) that employ compact and low power automotive grade MEMS inertial sensors and manage their larger drifts with zero velocity measurements on each footfall. Magnetic attitude sensing vs. MEMS gyroscopes are typically used in these systems. There is no mechanism in the foot mounted system architecture to control heading gyro drift. Reference [21] proposed a novel approach to controlling foot mounted gyro drift – use of foot-to-foot RF range measurements. Similar to foot sensor based ZUPT measurements, RF ranging gives observability into heading gyro drift on each footstep and enables use of compact automotive grade MEMS gyros for precision GPS-denied pedestrian navigation.

There are two challenges for all approaches that employ foot-mounted sensing. First responders and dismounted soldiers have low tolerance for any boot mounted instrument that interferes with operational mobility. Ideally all instrumentation should be mounted conformally on the boot or embedded in the heel in a way that does not affect walking dynamics. Secondly, hard-wired interconnects between boot and mid-body or pack mounted equipment are not desirable. The goal in this foot mounted design space is a highly compact, human motion powered suite of navigation sensors.

Optical Sensors

Recent innovations in navigation systems in GPS denied environments have included the addition of optical sensors as part of the overall instrumentation integration suite [Ref 32, 33]. Different types of optical sensors are employed to furnish specific types of aiding information to the navigation system algorithms. For example, common CCD cameras have been used to provide 2D image data for feature-based aiding (i.e. the identification of landmarks). Alternatively, laser scanners have been employed to add ranging information and elevation/azimuth angular orientation with respect to neighboring surfaces.

References [32, 33] discuss the optical sensor integration approaches in detail. In summary, feature-based navigation algorithms use cameras to identify landmarks, and correlate the location of their features over successive frame captures as an aiding method. In contrast, direct range and orientation (i.e. heading vector) information is furnished to the navigation solution with scanner-based instruments.

Recently, 3-D camera technology has emerged which combines both features of a conventional 2-D imaging array plus a rangefinder. Figure 22 below depicts the basic operational principle of 3-D cameras, and contrasts this approach with the “3-D” imaging approach used in stereoscopic implementations. The conventional stereoscopic method uses a pair of 2-D cameras to triangulate the range to a point common in both cameras fields of view.

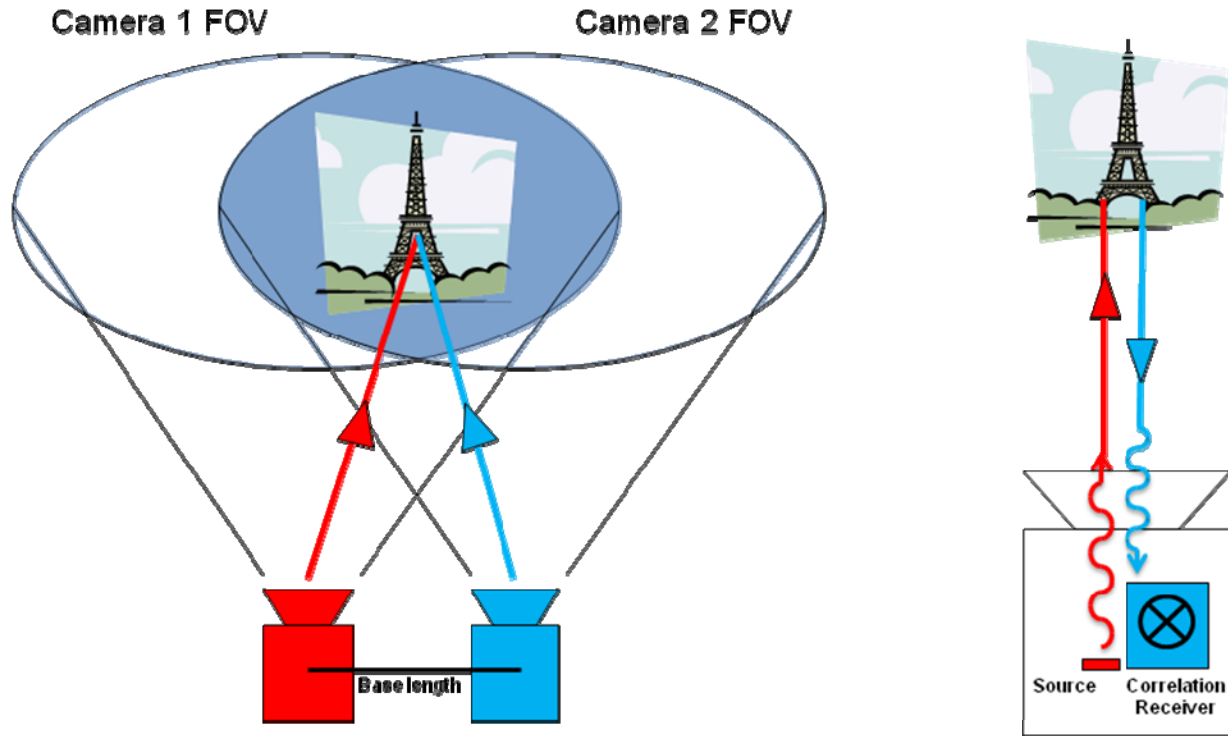


Figure 22: Stereoscopic 3-D imaging v. 3-D camera technology.

The 3-D camera integrates a laser source with the CMOS imaging array. The laser emits infrared spectrum energy, either as a pulse or as a continuously modulated waveform, which illuminates objects in the field of view. The time of flight for the laser pulse to return is captured and correlated with each pixel on the imaging array, furnishing both feature image and depth information in real time.

The emerging CMOS imaging technology has been critical to the development of 3-D cameras. In contrast with the more mature CCD technology, where the photon to charge conversion is sequentially captured and transported to voltage conversion electronics, CMOS technology enables direct photon to voltage conversion locally at each pixel element. This enables an advanced imaging chip architecture with enhanced functionality at the pixel level. 3-D cameras exploit this CMOS advantage by employing a dual-receptor pixel design that is electronically sampled as an in-phase and in-quadrature differential pair. Figure 23 below shows how this approach reconstructs range information.

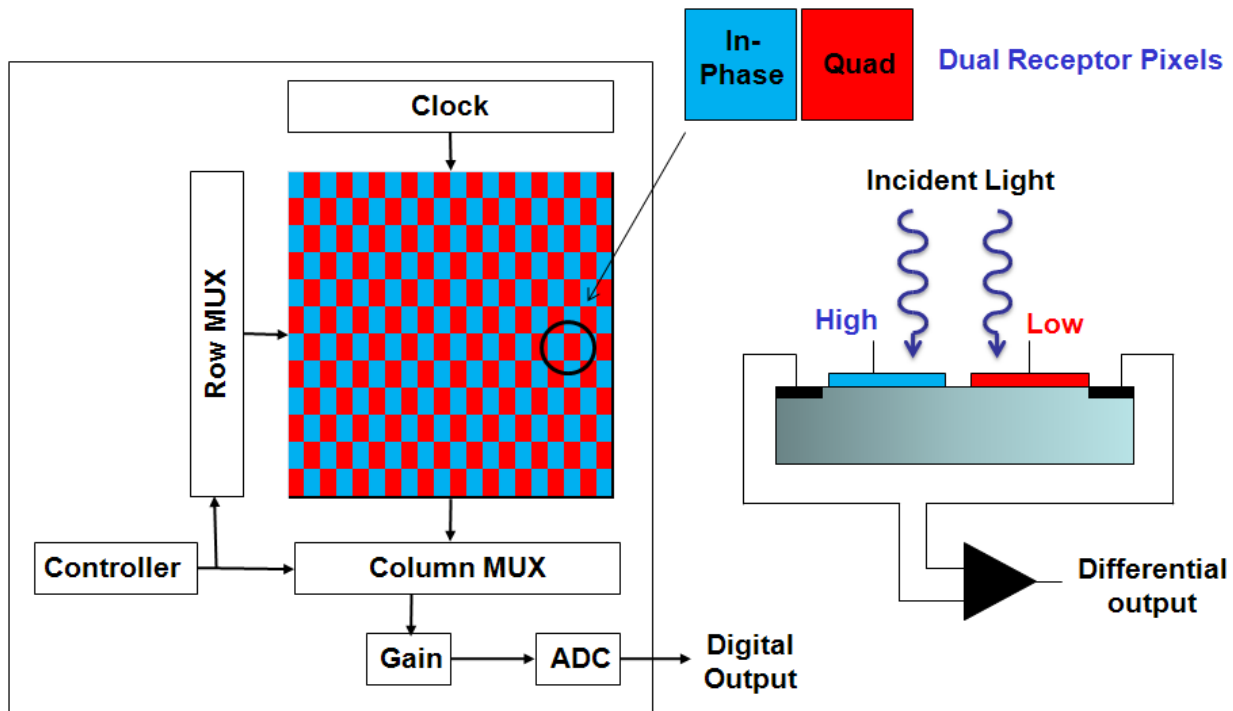


Figure 23: Dual Pixel Arrays for 3-D Imaging.

As shown, each pixel element consists of a pair of photo-sensitive elements. The camera has an optical source, a laser or LED, that illuminates objects in the field of view. The reflected light is absorbed by the dual pixel elements. The High/Low gates are modulated with a voltage waveform synchronized with the light source. The return phase of the light determines the amount of charge collected in each output gate of the pixel; hence, the voltage difference between the pair indicates the range to the object being imaged.

The light sources used are typically in the near infrared portion of the spectrum and are generated either by a laser or by an LED. Source performance factors of importance are maximum optical power and efficiency, as well as high modulation frequency and modulation contrast (rise and fall time of modulation intensity). Recent advances in high power IR LEDs have enabled their introduction to this application. Table 2 below compares and contrasts the tradeoffs between LED and laser sources.

Table 2: Laser v. LED Sources.

Source Technology	Advantages	Disadvantages
Infrared LED	<ul style="list-style-type: none"> Linear electro-optical properties Integrated beam shaping optics 	<ul style="list-style-type: none"> Source diffusion Efficiency ~30% Modulation limit: 20 MHz – 30 MHz
Laser Diode	<ul style="list-style-type: none"> Diffraction limited FOV Efficiency ~ 50% Modulation limit > 100 MHz 	<ul style="list-style-type: none"> Complex modulation circuitry Phase stabilization Eye safety

Some simple performance calculations will further illuminate some of the optical source tradeoff considerations. Range is determined either by measuring time-of-flight (TOF) for an optical pulse to return from the illuminated target, or by measuring the phase shift from the modulated source reflection. Timing resolution on the order of a pico-second will enable sub-millimeter resolution:

$$d = c t = (3 \times 10^8 \text{ m / s})(10^{-12} \text{ s}) = 0.3 \text{ mm} \quad [12]$$

where: d = distance
 c = speed of light
 t = time

Likewise milliradian phase measurement resolution is needed to resolve millimeter range variation:

$$\phi = \frac{4 \pi f d}{c} = \frac{4 \pi (20 \times 10^6 \text{ Hz})(10^{-3} \text{ m})}{3 \times 10^8 \text{ m / s}} = 0.84 \text{ mrad} \quad [13]$$

where: ϕ = phase
 d = distance
 c = speed of light
 f = modulation frequency

The modulation frequency determines the maximum range that can be measured unambiguously, that is, the distance the source waveform travels before cycling through 360° of phase angle:

$$NAR = \frac{c}{2 f} = \frac{3 \times 10^8 \text{ m / s}}{2 (20 \times 10^6 \text{ Hz})} = 7.5 \text{ m} \quad [14]$$

where: NAR = Non-Ambiguity Range
 c = speed of light
 f = modulation frequency

Additional details on performance metrics and calculations can be found in reference [38]. Among them is the ability to suppress ambient background illumination from saturating the dynamic range of the imaging array. In typical daylight applications, the ratio of the background sunlight to the 3D camera source intensity can exceed 80 dB (Ref [39]). Spectrally filtering the return light and operating the source in a burst mode to increase intensity offers only marginal improvement in the optical signal to noise ratio. Consequently, array developers have devised methods for actively suppressing ambient light “noise”. These techniques use additional signal processing at the local pixel level, enabled by the CMOS technology. Reference [39] describes one approach used to suppress background illumination, which exploits the uncorrelated relationship between the background noise and the 3D camera infrared source. The correlated signal can be augmented by injecting additional charges in the readout terminals, displacing the uncorrelated background charge and thus reducing the background noise.

Figure 24 below shows some 3D cameras offered by PMDTechnologies (Siegen, Germany, partnered with ifm electronic GmbH, Essen Germany) and MESA Imaging AG (Zurich, Switzerland). Canesta, Inc. (Sunnyvale, CA) also offers specialty made-to-order 3d camera products.



Figure 24: MESA Imaging & PMDTechnologies 3D Cameras.

Table 3. below summarizes some of the key parameters of the camera models shown in figure z.

Table 3: 3D Camera Model Comparison.

Parameter	MESA SR4000	PMD [vision]™ 03	PMD CamCube 3.0
Size (L x W x H)	65 mm x 65 mm x 68 mm	60 mm x 42 mm x 53.5 mm	60 mm x 60 mm x 60 mm
Range	0.8 m – 5.0 m	7.5 m (max)	0.3 m – 7.0 m
Repeatability	< 7 mm	< 20 mm	< 3 mm
Frame Rate	54 fps (max)	25 fps (max)	40 fps – 80 fps
FOV (H x V)	43.6° x 34.6°	30° x 40°	40° x 40°
Wavelength	850 nm	850 nm	870 nm

In contrast with the other augmentation sensors discussed in this paper, these example cameras are not, strictly speaking, “miniature”. They are reasonably compact and the imaging array sizes are typically less than a square centimeter. With the emergence of small LEDs and miniature optics, insertion of 3D imaging in a miniaturized navigation system is feasible, though would require a significant effort to integrate all the components in an efficient form factor.

GPS-UNAVAILABLE MISSION ANALYSES

Inertial technology development continues to be very active, and that the opportunity to reduce size while maintaining or even improving performance exists. In an attempt to relate these developments to GPS-unavailable missions, current and developing gyro and accelerometer technologies have been paired to optimize performance, and are shown in Table 4 below with projections on IMU size, weight and power. These IMU performance projections are used as a basis to perform a comparative analysis to see what benefits are to be gained from the technologies under development, and to assess the need for and benefit of navigation solution augmentation.

Table 4: Inertial Technology Performance Goals.

	Current Tactical- Grade IMUs	Nav-Plus	Ultra-High
<u>Gyro</u>			
Bias Stability (°/h)	1	0.001	0.0001
SF Stability (ppm)	300	1	5
ARW (°/√h)	0.1	0.0001	4×10^{-6}
<u>Accel</u>			
Bias Stability (μg)	1,000	1	0.1
SF Stability (ppm)	300	1	0.1
VRW (ft/s / √h)	0.2	0.001	10^{-5}
<u>IMU</u>			
Volume (cu. in)	4 - 35	8	4
Weight (lb)	2	2	0.3
Power (w)	12	5	5

In the simulation analyses below, the three representative IMUs spanning the low, high, and very high performance ranges, were selected from Table 4: 1) a current tactical grade IMU, 2) a hypothetical IMU representative of high performance, navigation grade sensors (“Nav-Plus”) and 3) a hypothetical IMU containing ultra-high performance inertial sensors. The RMS position, velocity, and attitude errors were initialized to zero. Three simulation cases were run: 1) Inertial with baro-altimeter, 2) Inertial with baro-altimeter and velocity meter, and 3) Inertial with baro-altimeter and intermittent availability of GPS. No magnetometer was incorporated in these simulations. The simulation plots show navigation error as a function of time.

The assumed trajectory was a random walk generated using an RMS heading rate parameter of 0.005 rad/s/√s. Thus these simulations do not reflect a particular mission, but are for comparison purposes only. Maximum speed is 1 meter/s and mission time is 8 hours. The velocity meter is assumed to give valid velocity readings for only some percentage of the time. It is assumed that bad readings are detected perfectly and not used. The velocity meter controls the low-frequency drift of the inertial solution, and is assumed to have an RMS error (white noise) of 3 cm/s/√s. The baroaltimeter stabilizes the inertial navigation in the vertical direction and is assumed available throughout with an RMS error (white noise) of 2 meters and altitude readings at one second intervals.

Inertial w/Baroaltimeter Solution

For an inertial-alone solution, none of the technologies under development can meet all the mission requirements of Table 1. This is shown in the simulation results in Figure 25. After only 30 minutes the position error would be 24,000 meters, 24 meters, and 2.4 meters with a tactical grade IMU, a Nav-Plus grade IMU, and an ultra-high performance IMU respectively. After 8 hours the respective errors would be 120,000 meters, 120 meters, and 12 meters. Only the ultra-high quality IMU meets the position knowledge requirements of 3 to 10 meters in Table 1 for a substantial amount of time. In all cases, the down error was maintained at a value comfortably below the accuracy requirement via use of the baro-altimeter.

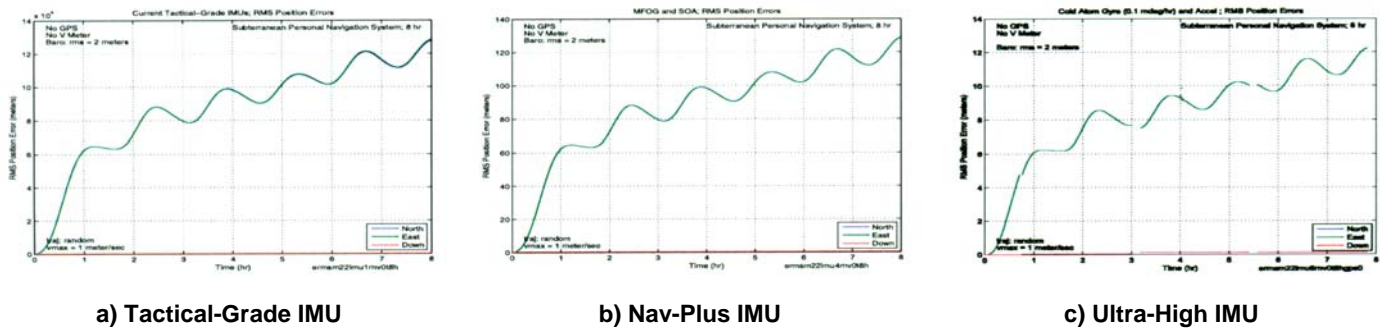


Figure 25: Inertial-only Solution - No Velocity Meter.

Inertial with Baroaltimeter plus Velocity Meter

Figures 26 through 28 show simulation results when a velocity meter is included. The tradeoff parameter is the probability of a good velocity measurement at each time step (one second increments) for each axis (denoted $p_v(on)$ in the plots). Simulated probabilities are for $p_v(on)$ equal to 0.03, 0.10, and 0.50. The probabilities are independent over axes, so that one, two or three axes could have bad measurements at the same time step. Figure 26 shows error spiking (sometimes to very high values) for the current tactical-grade IMU at low probability levels; this is attributable to significant periods of measurement outage. Note that the position error is reduced after the spikes; this is due to the correlations built up between position and velocity during the period of the spike, which is used to reduce position errors when good measurements are subsequently obtained from the velocity meter. This error spiking vanishes with the Nav-Plus IMU (Figure 27) and the Ultra-High Performance IMU (Figure 28) even at very low probability levels.

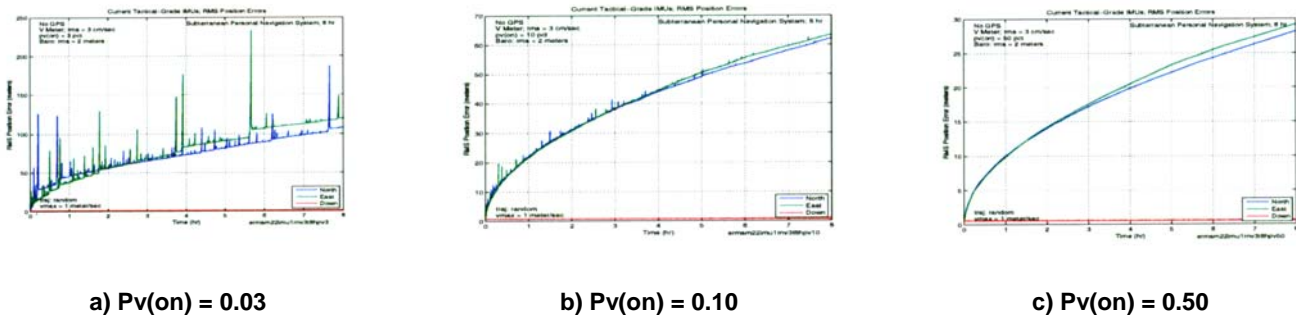
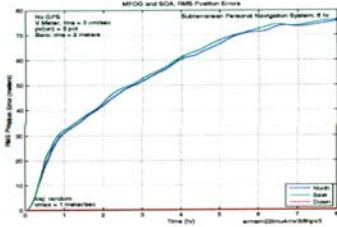
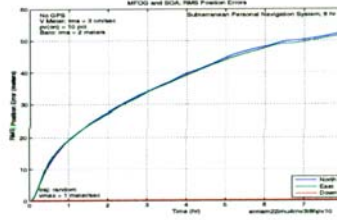


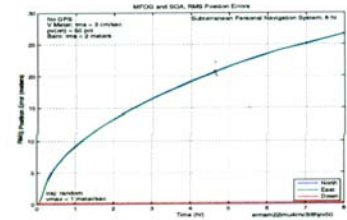
Figure 26: Current Tactical-Grade IMU.



a) $Pv(on) = 0.03$

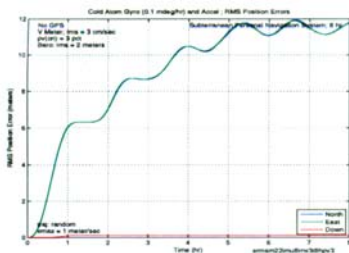


b) $Pv(on) = 0.10$

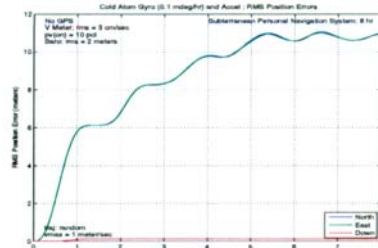


c) $Pv(on) = 0.50$

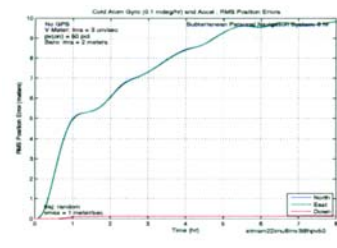
Figure 27: Nav-Plus IMU.



a) $Pv(on) = 0.03$



b) $Pv(on) = 0.10$



c) $Pv(on) = 0.50$

Figure 28: Ultra-High IMU.

When a velocity meter is used, it dominates in the ability to maintain high accuracy; there is only a slight reduction in rms position error after 8 hours using the nav-Plus IMU compared to a current tactical-grade IMU (~26 meters vs. ~28 meters along North and East for the case $Pv(on) = 0.50$). Even with a velocity meter none of the inertial technologies meets the 1 to 3 meters position knowledge requirements in Table 1 for more than a few minutes. All the technologies can meet the 10 meter requirement for at least one hour with $p_v(on)$ at 50 percent. Therefore, the major driver for improving the performance of the IMU would be to eliminate or reduce the intermittent position error spikes, when the velocity meter has low probability of providing accurate measurements. For an ultra-high performance IMU, comparison of Figures 28c and 25c show that the velocity meter smooths the inertial solution, but has little effect on average position error (~10 meters vs. ~12 meters inertial-alone).

Inertial with Baroaltimeter plus Intermittent GPS

Figure 29 shows the simulation results for three IMUs with no velocity meter, but with intermittent GPS availability, as in an autonomous land vehicle mission. GPS is assumed to be available such that one three-axis measurement of position and velocity is obtained every 120 s. The GPS signal allows the navigation solution to be bounded. The benefits of high performing IMUs for meeting the mission requirements in Table 1 are clearly evident in this situation.

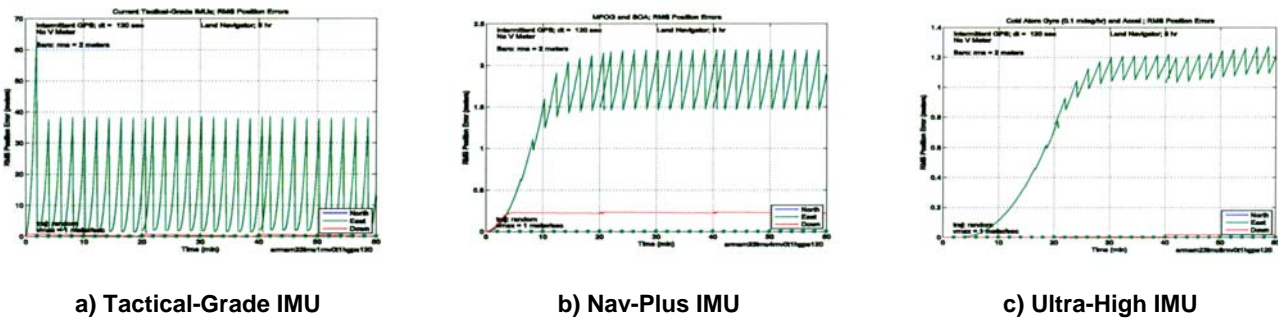


Figure 29: Autonomous Land Vehicle, Intermittent GPS – 1 Hour.

INTEGRATED NAVIGATION: PPS EXAMPLE

Draper Laboratory has developed a prototype integrated Personal Positioning System (PPS) for the US Army under the Future Force technology demonstration project (Ref [16, 27, 31]). This wearable, personal navigation system (Fig. 30) serves as a test case for the integration techniques and simulations discussed above, and contains the following hardware elements: 1) a tactical grade MEMS IMU, 2) P(Y) code GPS receiver, 3) W-band mm wave Doppler velocimeters, 4) baro-altimeter, and 5) 3-axis magnetometer. The embedded navigation filter implemented the deep integration GPS algorithm described in ref [16]. Measurements from all augmentation sensors, including GPS were screened before being allowed to affect the navigation sensor fusion. This screening, based on the well characterized error dynamics of the inertial sensors, was particularly important for eliminating GPS range measurements corrupted by multipath.

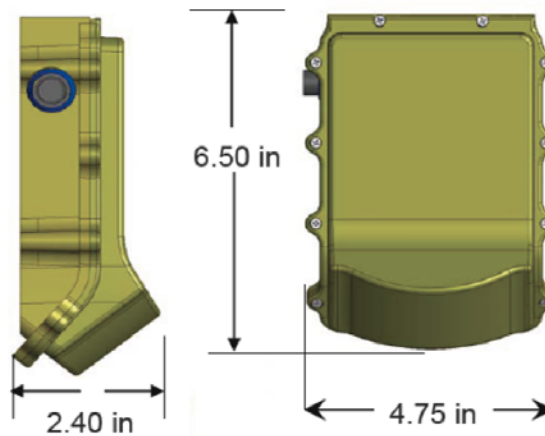
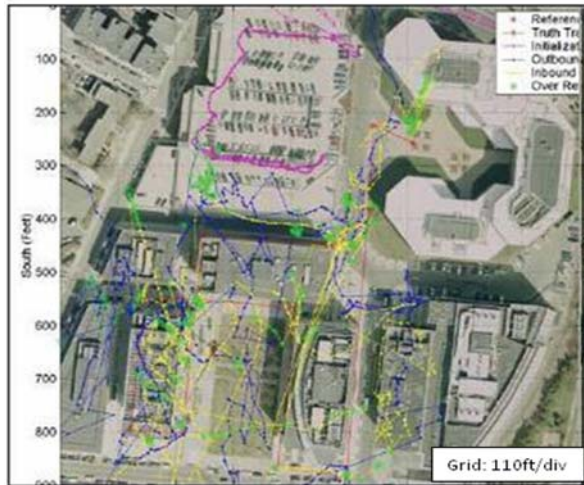


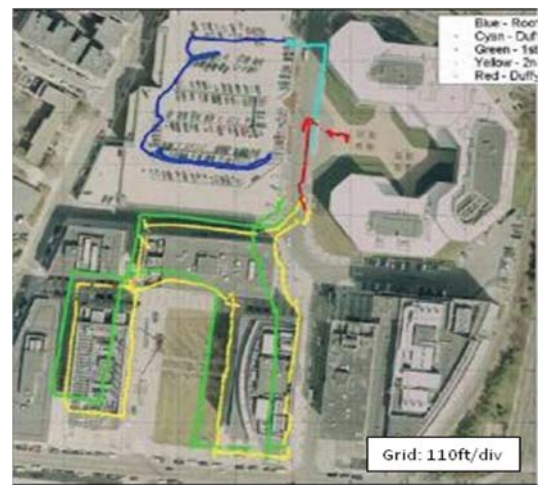
Figure 30: Prototype Integrated Personal Positioning System (PPS) (Ref. [27]).

The Draper PPS was evaluated on two test courses: 1) an “Urban Canyon” test area with severe GPS satellite line-of-sight obstruction and multipath and 2) on an eight floor office building indoor course to characterize performance across an outdoor-indoor-outdoor transition. The course was surveyed to furnish a true position reference for score against the PPS indicated position.

Figures 31 and 32 show navigation results on the outdoor urban canyon track, contrasting the poor results from a GPS-only solution against the computed position from the PPS. The benefits of sensor augmentation are obvious here as the multi-path and GPS signal loss effects evident in fig. 31 are mitigated in the PPS system.



**Fig 31. "Urban Canyon" Navigation:
GPS Only (Ref [27]).**



**Fig 32. "Urban Canyon" Navigation:
Integrated PPS (Ref [27]).**

Additional "Urban Canyon" trials are shown below in figs 33. The color coding of the tracks indicate the number of GPS satellites available to the navigation filter: blue corresponds to 4 or more satellites in view, cyan 3, yellow 1 and red indicates no GPS at all. Accuracy results are tabulated below the figures.

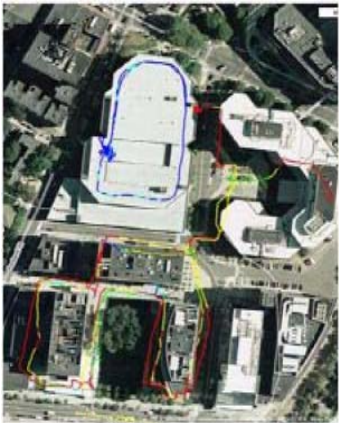

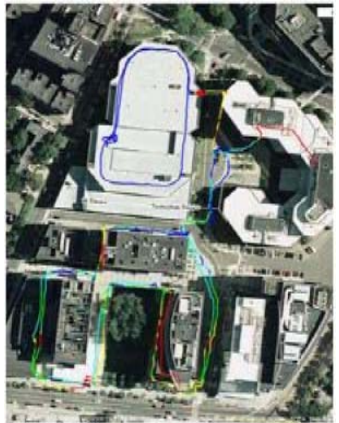
		
Trial 1	Trial 2	Trial 3
Horizontal Error (m)	Horizontal Error (m)	Horizontal Error (m)
50% - 5.2	50% - 3.6	50% - 3.2
RMS - 7.2	RMS - 4.6	RMS - 4.2
Vertical Error (m)	Vertical Error (m)	Vertical Error (m)
50% - 8.2	50% - 7.5	50% - 3.6
RMS - 8.8	RMS - 7.6	RMS - 4.1

Figure 33: PPS Test Results: Urban Canyon Track (Ref. [27]).

Figure 34 shows results from the outdoor-indoor-outdoor transition trials (ref [27]). Indoor performance over 20 minutes of GPS denial was consistent with predictions from simulations in Figure 22c; CEP error over 12 runs was about 5 m. This included “stress” scenarios that exercised position and heading initialization under GPS challenged conditions.



Figure 34: Indoor Navigation with Integrated PPS (Ref. [27]).

Analysis of the results indicate that the indoor performance error was dominated by position and heading initial condition errors at entrance to the building.

For multi-sensor navigator design, a key and often under-appreciated IMU parameter is the characteristic time associated with IMU error state stability. The design philosophy is to construct a navigator to operate on high

quality but intermittent augmentation measurements which as a group give complete observability onto IMU error states. A higher level of error stability, with a tolerance for sparser augmentation, can come from careful sensor packaging and thermal management of lower quality inertial instruments. This path, in the short term, will likely lead to a more compact and lower power system. A takeaway of the simulations in this section is that angle random walk, which is usually the focus of new sensor design, is not always the dominant parameter in system performance.

SUMMARY

A survey on magnetometers, velocity meters, barometers, optical sensors and timing sources was presented, with an emphasis placed on identifying accurate, miniature versions of these sensors that are currently available or well along in development. Simulations showed that the addition of these segmentation sensors can suppress position error growth under GPS-denied situations when integrated properly into the navigation solution. It is only when inertial performance on the order of 0.001 deg/hr, and 1 micro-g is available that the some of the reliance on other aiding schemes can be relaxed in GPS-denied situations; currently this level of performance is not available in miniature inertial sensors.

Simulations indicate the inclusion of a velocity meter to augment the inertial solution significantly improves accuracy over short periods of time in the GPS-denied environment. This was demonstrated experimentally during testing of a Draper lab prototype personal navigation system. The Draper PPS system, an integration of a MEMS tactical grade IMU, P(Y)-Code GPS, magnetometer, barometer and Doppler velocity meter, demonstrated better than 5 m position accuracy in urban canyon and GPS-denied indoor testing.

ACKNOWLEDGEMENTS

This paper is an updated version of the paper “Miniature Inertial and Augmentation Sensors for Integrated Inertial/GPS based Navigation Applications” by Hopkins, Barbour, Gustafson, Sherman, published in the proceedings of the NATO SET 116 symposium (Ref. [30])

REFERENCES

- [1] Datasheet: Integrated Guidance Systems website:
<<http://www.igsllc.com/docs/IGS2xx%20Data%20Sheet%200509.pdf>>.
- [2] Datasheet: Atlantic Inertial Systems website:
<http://www.atlanticinertial.com/uploads/pdfs/SINAV02_07.pdf>.
- [3] Barbour N., *Inertial Navigation Sensors (SET116)*, NATO RTO SET116 Symposium on Low Cost Navigation Sensors, December 2008, March 2009, March 2010.
- [4] Kitching J., *Chip Scale Atomic Devices, Precision Instruments based on Lasers, Atom and MEMS*, Microsystems Technology Symposium, San Jose CA, March 2009.
- [5] Press Release: 1 November 2007: New NIST Mini-Sensor May Have Biomedical and Security Applications, *Ultrasensitive Prototype Device Approaches Gold Standard for Magnetic Field Detection*, Contact info: Laura Ost, (303) 497-4880, www.nist.gov.

- [6] Strangeway R., 11 June 2001, *Fluxgate Magnetometer for NASA/GSFC ST5 Mission*, <http://dawn.ucla.edu/st5/design.html>.
- [7] PNI Sensor Corporation, 133 Aviation Blvd., Suite 101, Santa Rosa, CA 95403-1084, www.pnicorp.com.
- [8] McLean, S., S. Macmillan, S. Maus, V. Lesur, A. Thomson, and D. Dater, December 2004, *The US/UK World Magnetic Model for 2005-2010*, NOAA Technical Report NESDIS/NGDC-1, http://www.ngdc.noaa.gov/geomag/WMM/data/TRWMM_2005.pdf
- [9] Technical Articles: Magnetic Sensor Overview: <<http://www.honeywell.com/sites/>>.
- [10] Biezd D., *Integrated Navigation and Guidance Systems*, AIAA Education Series, © 1999.
- [11] Savage P., *Introduction to Strapdown Inertial Navigation Systems*, Strapdown Associates, © 1996.
- [12] Groves P., *Principles of GNSS, Inertial, and Multisensor Integrated Navigation Systems*, Artech House, © 2008.
- [13] Seo J. et al, *Bias Suppression of GPS Measurement in Inertial Navigation System Vertical Channel*, Proc. of IEEE/ION PLANS, pp. 143-147, April 2006.
- [14] VTI Technologies website: www.vti.fi.
- [15] Chang D., *Miniature Coherent Velocimeter and Altimeter (MCVA) for the Terminal Descent Control on Lunar and Planetary Landers*, JPL Manuscript.
- [16] Landis D. et. al, *A Deep Integration Estimator for Urban Ground Navigation*, IEEE PLANS 2006, 0-7803-9454-2.
- [17] Lal A. et. al, *Velocity Sensor Assisted Micro Inertial Measurement for GPS Denied Personal Navigation*, Joint Navigation Conference (JNC) 2009, Orlando, FL, June 2009.
- [18] L. Ojeda and J .Borenstein, *Non-GPS Navigation for Emergency Responders*, 2006 International Joint Topical Meeting: “Sharing Solutions for Emergencies and Hazardous Environments”.
- [19] Website: www.g-trax.com.
- [20] E. Foxlin, NavShoe™ Pedestrian Inertial Navigation Technology Brief, 2006 WPI Workshop on Precision Indoor Personnel Location and Tracking for Emergency Responders.
- [21] Brand T. et. al, *Foot-to-Foot Range Measurement as an Aid to Personal Navigation*, Proc. ION 59th AM. Albuquerque, NM, pp. 113-125, June 2003.
- [22] Lutwak R. et al, *The MAC - A Miniature Atomic Clock*, Joint IEEE International Frequency Control Symposium and Precise Time and Time Interval (PTTI) Systems and Applications Meeting, Vancouver, BC, Canada, August 2005.
- [23] Mescher M. et al, *An Ultra-Low-Power Physics Package for a Chip Scale Atomic Clock*, Transducers 05, Seoul, Korea, June 2005.

- [24] Lutwak R., *The Miniature Atomic Clock – Pre-Production Results*, IEEE Frequency Control Symposium, May 2007.
- [25] Knappe S., *Emerging Topics: MEMS Atomic Clocks*, in Y. Gianchandani, O. Tabata, and H. Zappe (eds.) *Comprehensive Microsystems*, Elsevier, Netherlands, 2007.
- [26] Datasheet: <www.ssec.honeywell.com/magnetic/datasheets/hmc1043.pdf>.
- [27] Sherman, P., et. al., *Precision Positioning System –Autonomous GPS-Denied Navigation for the Dismounted Soldier*, WPI Indoor Personnel Location and Tracking for Emergency Responders, August 4-5, 2008.
- [28] http://www.gemsys.ca/Technology/Papers/GEM_Brief_Review_of_Quantum_Magnetometers.pdf.
- [29] Kayton M., Fried W. (eds) *Avionics Navigation Systems*. 2nd edition, Wiley, 1997.
- [30] Barbour N. Gustafson D., Hopkins R., Sherman P., *Miniature Inertial and Augmentation Sensors for Integrated Inertial/GPS Based Navigation Applications*, NATO RTO SET116 Symposium, Low Cost Navigation Sensors and Integration Technology, March 2010.
- [31] Sherman P., Holmes S., *Personal Navigation System*, Technical Report Natick/TR-06/004, October 2005.
- [32] Miller M., Uijt de Haag M., Soloviev A., Veth M., Klausutis T. Touma J., *Navigation in GPS Denied Environment: Feature Aided Inertial Systems*, NATO RTO SET116 Symposium, Low Cost Navigation Sensors and Integration Technology, March 2010.
- [33] Miller M., Uijt de Haag M., Soloviev A., *Navigation in Difficult Environments: Multi-Sensor Fusion Techniques*, NATO RTO SET116 Symposium, Low Cost Navigation Sensors and Integration Technology, March 2010.
- [34] Robertson P., Angermann M., Krach B., Khider M., *SLAM Dance: Inertial-Based Joint Mapping and Positioning for Pedestrian Navigation*, InsideGNSS, May 2010, www.insidegnss.com.
- [35] Robertson P., M., Krach., *Cascaded Estimation for Integration of Foot Mounted Inertial-Sensors* Proceedings IEEE PLANS 2008, Monterey CA, May 5-8 2008.
- [36] Campbell J., Miller M., Uijt de Haag M., Venable D., Smarcheck M., *Flash-LADAR Inertial Navigator Aiding*, Proceedings IEEE PLANS 2006, Coronado CA, May 5-8 2006.
- [37] Ringbeck T., *A 3-D Time of Flight Camera for Object Detection*, Optical 3-D Measurement Techniques 09-12.07.2007 ETH Zurich, Plenary Session I: Range Imaging I.
- [38] *A performance review of 3-D TOF vision systems in comparison to stereo vision systems*, White Paper, PMDTechnologies GmbH, Am Eichenhang 50, D-57076 Siegen, www.PMDTec.com.
- [39] Moller T., Kraft H., Frey J., Albrecht M., Lange R., *Robust 3D Measurement with PMD Sensors*, Range Imaging Day, Zurich, 2005.

